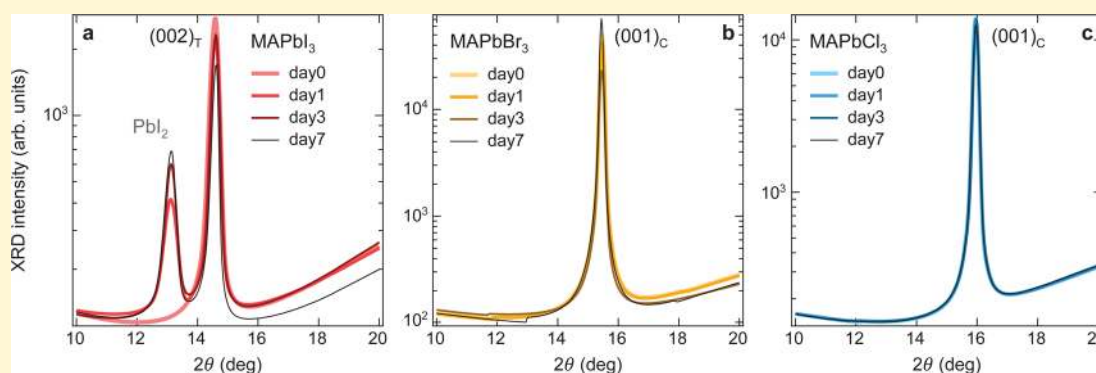# Halide-Dependent Electronic Structure of Organolead Perovskite Materials

Andrei Buin, Riccardo Comin, Jixian Xu, Alexander H. Ip, and Edward H. Sargent*

Department of Electrical and Computer Engineering, University of Toronto, Toronto, Ontario, Canada M5S 3G4

ABSTRACT: Organometal halide perovskites have recently attracted tremendous attention both at the experimental and theoretical levels. These materials, in particular methylammonium triiodide, are still limited by poor chemical and structural stability under ambient conditions. Today this represents one of the major challenges for polycrystalline perovskite-based photovoltaic technology. In addition to this, the performance of perovskite-based devices is degraded by deep localized states, or traps. To achieve better-performing devices, it is necessary to understand the nature of these states and the mechanisms that lead to their formation. Here we show that the major sources of deep traps in the different halide systems have different origin and character. Halide vacancies are shallow donors in I-based perovskites, whereas they evolve into a major source of traps in Cl-based perovskites. Lead interstitials, which can form lead dimers, are the dominant source of defects in Br-based perovskites, in line with recent experimental data. As a result, the optimal growth conditions are also different for the distinct halide perovskites: growth should be halide-rich for Br and Cl, and halide-poor for I-based perovskites. We discuss stability in relation to the reaction enthalpies of mixtures of bulk precursors with respect to final perovskite product. Methylammonium lead triiodide is characterized by the lowest reaction enthalpy, explaining its low stability. At the opposite end, the highest stability was found for the methylammonium lead trichloride, also consistent with our experimental findings which show no observable structural variations over an extended period of time.

Research in organometal halide solar cells has been burgeoning in the past few years following recent breakthroughs in power conversion efficiencies (PCE).[1,2] Most research studies[3−12] focused on methylammnonium (MA) lead triiodide (MAPbI$_3$) perovskite because of its optimal bandgap and its compatibility with solution-based processing. Br-based perovskites have also garnered interest,[13−16] whereas pure Cl-based perovskites have been explored to a limited extent. Br- and Cl-based platforms, thanks to their wider bandgap, hold great promise in the fields of photo-catalysis and photodetection.

It is known that Br/Cl-perovskites are more stable under ambient conditions, whereas it was shown that the introduction of Cl during MAPbI$_3$ formation enhances the performance of photovoltaic devices.[17] This raises important questions regarding the mechanisms that control the stability and defect physics in the different halide perovskites. In this work we explore the effect of halide replacement in organolead perovskite materials. Particularly, we focus on the defect physics of halide perovskite phases MAPbX$_3$ including X = I,

Cl, Br and the possible role of Cl in the MAPbI$_3$ perovskite. In addition, we analyze the stability of perovskite compounds in terms of reaction enthalpies with respect to precursor phases. Our results reveal remarkable differences between different halide systems, and suggest distinct optimal growth conditions for each perovskite system.

We performed density functional theory (DFT) calculations whose details can be found in the Methods section. The notation used for defect classification is as follows: vacancies (V$_{Pb}$, V$_X$), interstitials (Pb$_i$, X$_i$), and antisites (Pb$_X$, X$_{Pb}$), where in the latter case A$_B$ indicates that A is substituted by B and X is the halogen species (I, Br, or Cl). We have concentrated mainly on the metal-halide related defects, because their growth condition (halide-poor/halide-rich) can readily be controlled by choosing different lead halide precursors. We have
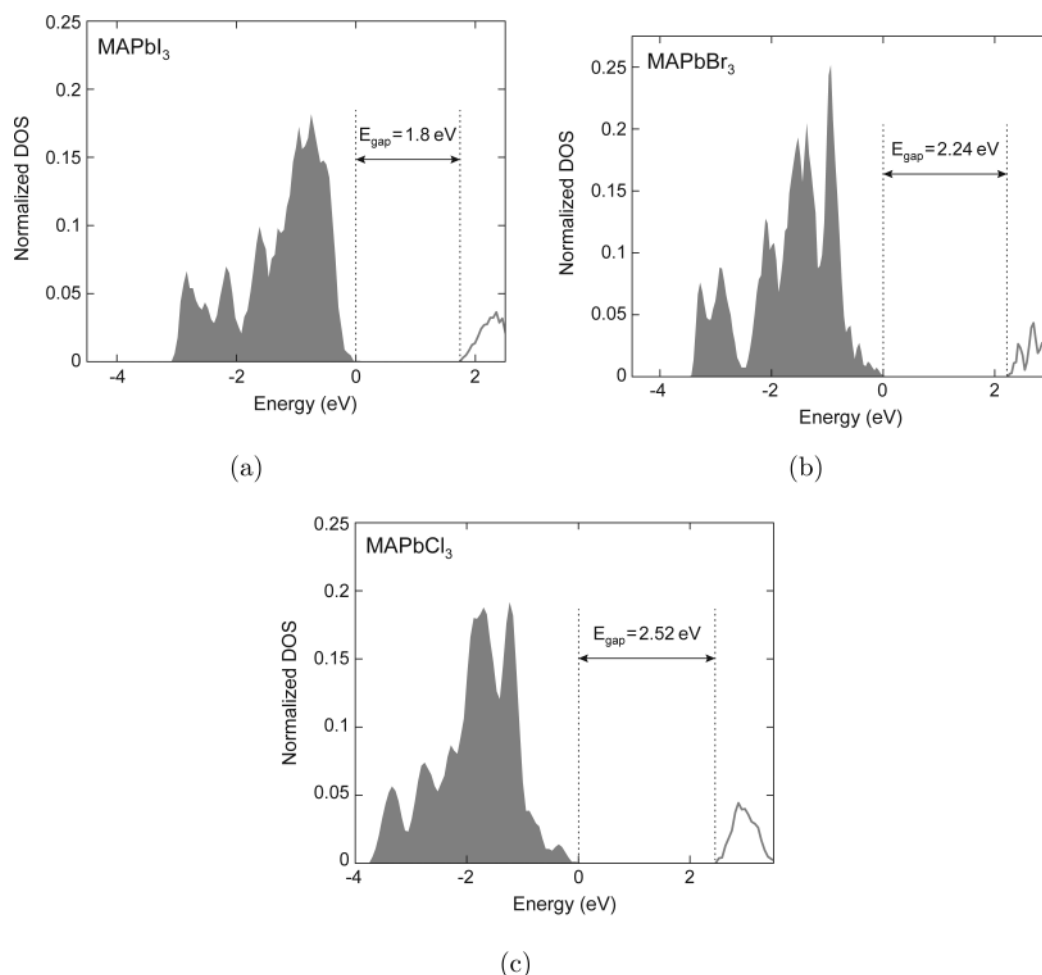
Figure 1. Normalized density of states (DOS) for: (a) tetragonal $MAPbI_3$; (b) cubic $MAPbBr_3$; (c) cubic $MAPbCl_3$.

concentrated mostly on the deep defects that were related to these lead-halide ions.[4,18,19]

To validate our model and correlate it to experimental results, we first calculated the density of states (DOS) of $MAPbX_3$. Figure 1 shows the density of states of the tetragonal $MAPbI_3$ and cubic $MAPbBr_3$ and $MAPbCl_3$ room-temperature phases. The bandgap is in line with experimental values[20] and follows the well-known trend going from I to Cl. The increase in bandgap is attributed to the decrease in lattice parameter along with a larger compressive strain[20] which leads to higher wave function overlap and, as a result, higher orbital coupling. Moreover, the differences caused by similarly sized cations,[21] i.e., formamidinium (FA) and MA cations, and different[22] crystal structures (tetragonal and cubic), can be ascribed to tilting of the PbI_6 octahedra. This tilting has an impact on the Pb−I bond lengths and angles, as these affect the wave function overlap, which leads to the change in bandgap. Further, because the VBM is built upon hybridization between Pb 6s and $X(3p_z,4p_z)$ orbitals with mainly $X(3p_z,4p_z)$ character, it is reasonable to expect that going from I to Cl, the weight of the X molecular orbitals (MO) should increase. This impacts the ionization potential (the HOMO with respect to the vacuum) as demonstrated in recent work of Butler et al.[23] Figure 2 shows the relative band alignment of $MAPbBr_3$ and $MAPbCl_3$ compounds with respect to $MAPbI_3$. To align them, we have used the common, deep-lying Pb 5d levels as a reference.[24] We find that the bandgap increment from I to Br to Cl is
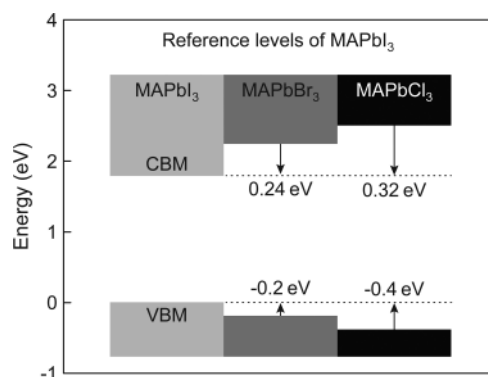

Figure 2. Band alignment among different organometal halide perovskites, with energy referencing to deep-lying Pb 5d levels. VBM (CBM) indicates the valence band maximum (conduction band minimum).

symmetrically driven by a concomitant downshift of the valence band and an upshift of the conduction band. This result is in good agreement with previously published results[23−25] on the alignment of the valence and conduction bands.

Next, we turn our attention to the defect physics in all three organometal halide systems. Although previous studies[4,11,18] have charted the defect levels of the $MAPbI_3$, reports are scarce for $MAPbBr_3$ or $MAPbCl_3$, motivating our theoretical study presented hereafter. The thermodynamic defect transition
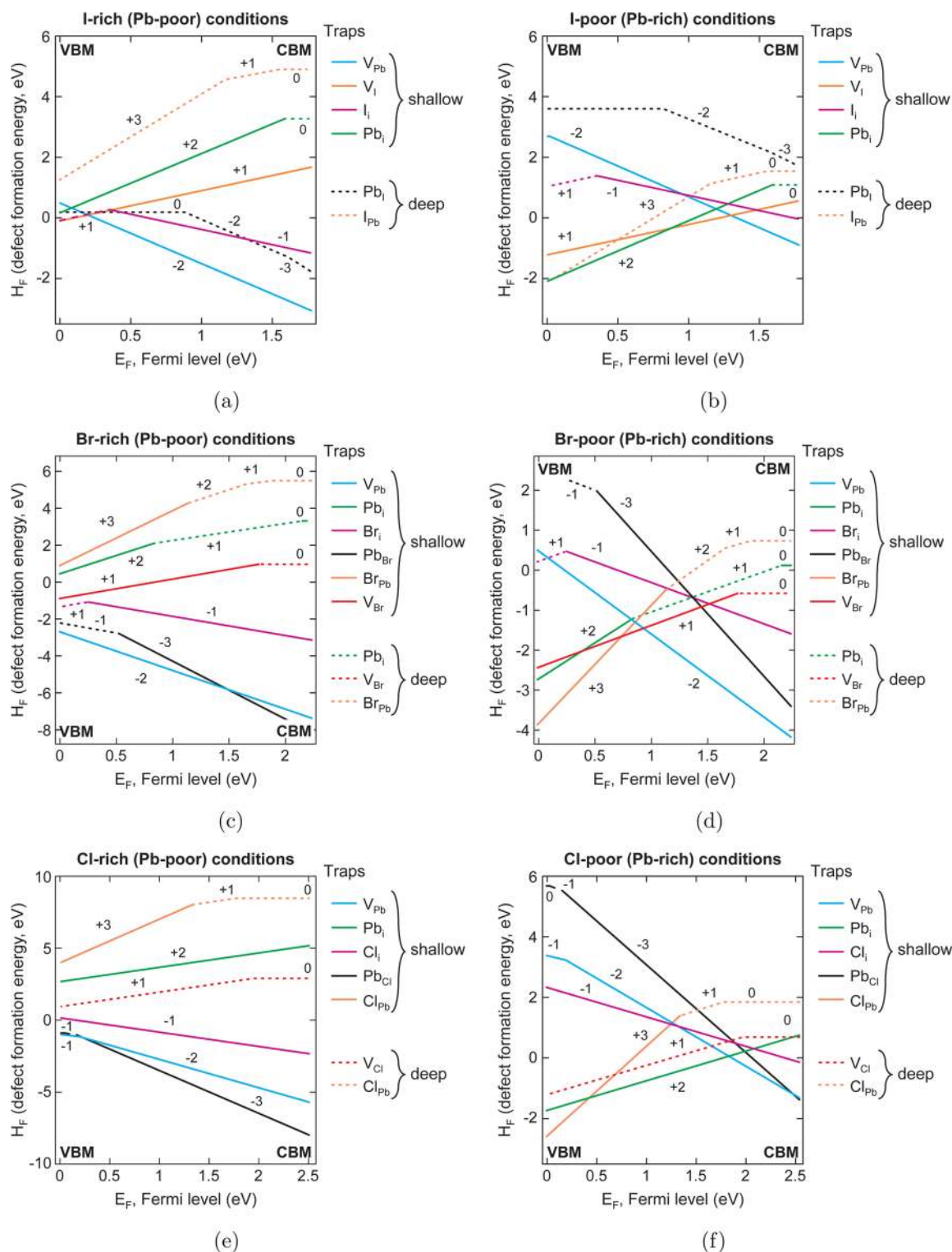
Figure 3. Defect formation energies under halide rich conditions for: (a) tetragonal MAPbI$_3$; (c) cubic MAPbBr$_3$; and (e) cubic MAPbCl$_3$ perovskite phases. Defect formation energies under halide-poor environments for: (b) tetragonal MAPbI$_3$; (d) cubic MAPbBr$_3$; and (f) cubic MAPbCl$_3$ perovskite phases.

levels are defined as points of equal formation energies[26] for different charged states. These levels are strong indicators of whether the defects states will be deep or shallow: deep for stable charged states over the bandgap; shallow for close-to-the-bandedge states. DFT eigenvalues are shown in Figure 3 as solid for near-bandedge states and dashed lines for in-gap states.

We then turned to examine the defect formation energy diagrams for halide-rich and halide-poor growth conditions. The two scenarios are presented in Figure 3: halide-rich (Pb-poor) on the left and halide-poor (Pb-rich) on the right. Given that strictly halide-rich and Pb-rich conditions would correspond to the halide precursor in solid (I$_2$), liquid (Br), or gaseous (Cl$_2$) form, and Pb in fcc form, respectively, they

rather serve as two extreme cases. Nonetheless, our analysis reveals which conditions halide-poor or halide-rich are preferable for the purposes of attaining a low trap density.

From Figure 3, it is apparent that in the case of MAPbI$_3$ and MAPbBr$_3$, the dominant defect under halide-rich conditions is the lead vacancy (V_{Pb}^{-2}). In the case case of MAPbCl$_3$, Pb_{Cl}^{-3} antisite is the dominant defect state. Surprisingly, the Pb_{Cl} antisite defect in cubic MAPbCl$_3$ is a shallow acceptor with a most stable charge state of -3. For this defect state, the situation is drastically different in the case of MAPbI$_3$, a fact which can be attributed to the fact that the tetragonal symmetry has a large relaxation energy (or large negative correlation energy U, negative U effect) that stabilizes the neutral state of the Pb_I antisite. This can be further clarified by looking at the work of Yin et al.[11] where no stabilization of the neutral state was found to occur in the cubic phase of the MAPbI$_3$. This is in line with our previous calculations,[4] where two unique Pb_I antisites have been identified, one of which (in-plane) is in close agreement with previously published work.[11] The lead antisites (Pb_{Br}, Pb_{Cl}) in the case of MAPbBr$_3$ and MAPbCl$_3$ are also defects with with -3 stable charge state and negative U behavior since the correlation energies are $U = -1.63$ eV and $U = -0.7$ eV, respectively. The correlation energies are defined as $U = \varepsilon(-1/-2) - \varepsilon(-2/-3)$, where ε is the thermodynamic transition level of the corresponding charged states. In the diagrams of Figure 3, thermodynamic transition levels occur at those locations where the first derivative has a discontinuity. Lead antisites in the case of cubic MAPbBr$_3$ and tetragonal MAPbI$_3$ phases possess a deep-trap character associated with formation of linear trihalide ions, i.e., Br_3^- and I_3^-. It is interesting to note that in the case of MAPbCl$_3$ and MAPbBr$_3$, trihalide ions are formed only with charged state -1, whereas in the case of MAPbI$_3$, triiodide ions can be formed with -3, -2, and -1 charged states. In the case of cubic MAPbBr$_3$ the Pb_{Br} antisite is a deep acceptor with very high thermal ionization energy,[26] in contrast with the case of MAPbCl$_3$, where the acceptor thermal ionization energy is very low.

In another major difference between tetragonal MAPbI$_3$ and cubic MAPbBr$_3$ and MAPbCl$_3$ phases, halide vacancies (V_{Br} and V_{Cl}) exhibit deep-trap behavior compared to V_I. This difference is attributed to the fact that transition level $\varepsilon(0/+1)$ of V_I in MAPbI$_3$ is located in the conduction band (CB),[4,11] leading to hybridization between singly occupied neutral defect state and states near the CB edge. As a result, it is resonance within the conduction band minimum (CBM). Figure 3 shows that the thermal ionization level $\varepsilon(0/+1)$ is found approximately 1.8 eV above the valence band maximum (VBM) for all halide vacancies (V_I, V_{Br}, V_{Cl}), thus leading to deep-trap behavior in MAPbBr$_3$ and MAPbCl$_3$ due to their wider bandgap. The wave function analysis of the V_{Br}^0 and V_{Cl}^0 states reveals localized σ bond hybridization between nearest neighbor $Pb(6p_z)$-$Pb(6p_z)$ orbitals and σ^* bond involving $Pb(6p_z)$-$X(3p_z,4p_z)$ orbitals as shown in Figure 4. The position of the defect state is affected by both the $Pb(p)$-$Pb(p)$ hybridization strength[27] as well as by flattening of the $[PbX_3]^-$ network[22] going from Br to Cl (which is reflected in angle X-Pb-X being equal to 164° and 166° for Br and Cl, respectively), which affects CBM location.[28]

Note that the interstitial defects (I_i, Br_i, Cl_i) are negative U defects but only the charge state $+1$ is stable and close to the VBM in the case of iodide and bromide perovskites. The localization ($X(4p,5p)$-$X(4p,5p)$, σ^*) and relaxation pattern of the X_i^+ states are very similar to those of the antisite defect, a
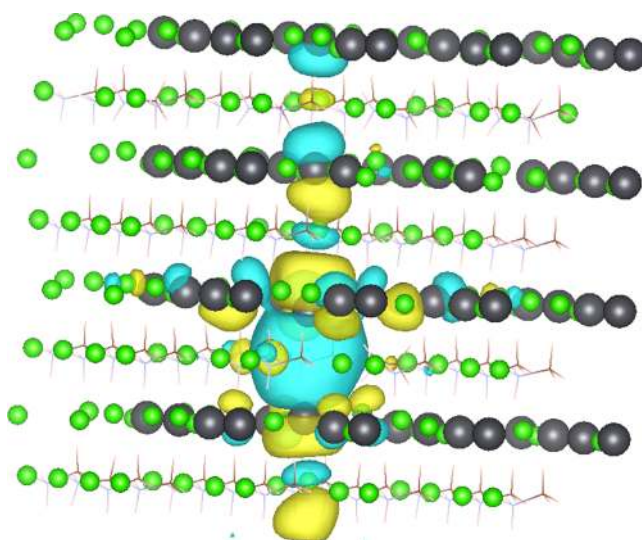

Figure 4. V_{Cl} deep state wave function. Gray atoms, Pb; green, Cl; sticks represent the MA cation. Positive lobe is indicated by blue, whereas negative lobe of the wave function is depicted by yellow color. It clearly shows σ-$Pb(6p_z)$-$Pb(6p_z)$ and σ^*-$Pb(6p_z)$-$Cl(3p_z)$ patterns.

finding that is in agreement with previously published[18] results. On the other hand, the thermodynamic transition level ($\varepsilon(-1/+1)$) of Cl_i is located inside the valence band of MAPbCl$_3$ leaving only charged state -1 stable over the entire bandgap.

In addition to individual defect states, we have also calculated the binding energy of complex defects such as Pb_X and X_{Pb} antisites for various charged states and according[29] to

$$E_b[(V_{Pb} + X_i)^q] = H_f[Pb_X^q] - H_f[V_{Pb}^n] - H_f[X_i^m] \quad (1)$$

$$E_b[(V_X + Pb_i)^q] = H_f[X_{Pb}^q] - H_f[V_X^n] - H_f[Pb_i^m] \quad (2)$$

where E_b is the defect binding energy, whereas H_f is the defect formation energy of the various defects in the various q, m, n-charged states, where $q = m + n$, X = I, Br, Cl. We adopt the convention that negative (positive) binding energies indicate stable (unstable) complexes. In addition, the reaction pathways for defect complexes are not unique, i.e., there are many possibilities to satisfy the condition $q = m + n$ as can be seen from Table 1, where, for example, Pb_{Br}^{-1} can have 3 possible decomposition pathways. It is important to note that the defect complex is stable only if all decomposition pathways are unfavorable. For example, in the case of the Pb_{Br} antisite, as can be seen from Table 1, the only complex that might appear stable is Pb_{Br}^{-1}; however, it would decompose into the most stable V_{Pb}^{-2} and Br_i^{+1}. Thus, no complexes are stable, i.e., Pb_{Br} decomposes into a lead vacancy (V_{Pb}) and a Br-interstitial (Br_i) and Br_{Pb} decomposes into a bromide vacancy (V_{Br}) and Pb-interstitial (Pb_i).

One should keep in mind that the above considerations do not imply that defect complexes such as Pb_{Br} and Br_{Pb} antisites will not be formed during perovskite crystallization.

These metastable defect complexes will form and their concentration will depend on the defect formation energy; however, they will tend to decompose by overcoming kinetic barriers through energy supplied via thermal annealing or light soaking. Br_i in the oxidation state $+1$ has a very narrow stability region in the case of extreme p-type doping; thus it is unstable over nearly the entire bandgap (intrinsic to lightly doped conditions). In case of the Br_{Pb} defect complex, Table 1 shows

Table 1. Defect Binding Energies for the Defect Complexes in MAPbI$_3$, MAPbBr$_3$ and MAPbCl$_3$ Perovskites

defect complex	decomposition	binding energy, eV
Pb$_{Br}^{-3}$	V$_{Pb}^{-2}$+Br$_i^{-1}$	2.358
Pb$_{Br}^{-1}$	V$_{Pb}^{-1}$+Br$_i^0$	−0.450
	V$_{Pb}^{-2}$+Br$_i^{+1}$	1.836
	V$_{Pb}^0$+Br$_i^{-1}$	−0.209
Br$_{Pb}^0$	V$_{Br}^0$+Pb$_i^0$	1.294
Br$_{Pb}^{+3}$	V$_{Br}^{+1}$+Pb$_i^{+2}$	1.329
Br$_{Pb}^{+2}$	V$_{Br}^{+1}$+Pb$_i^{+1}$	1.736
	V$_{Br}^0$+Pb$_i^{+2}$	0.620
Br$_{Pb}^{+1}$	V$_{Br}^0$+Pb$_i^{+1}$	1.562
	V$_{Br}^{+1}$+Pb$_i^0$	1.259
Pb$_{Cl}^0$	V$_{Pb}^0$+Cl$_i^0$	−0.421
Pb$_{Cl}^{-3}$	V$_{Pb}^{-2}$+Cl$_i^{-1}$	0.061
Pb$_{Cl}^{-1}$	V$_{Pb}^{-1}$+Cl$_i^0$	−0.419
	V$_{Pb}^{-2}$+Cl$_i^{+1}$	−0.344
	V$_{Pb}^0$+Cl$_i^{-1}$	0.011
Cl$_{Pb}^0$	V$_{Cl}^0$+Pb$_i^0$	−0.104
Cl$_{Pb}^{+3}$	V$_{Cl}^{+1}$+Pb$_i^{+2}$	0.333
Cl$_{Pb}^{+1}$	V$_{Cl}^0$+Pb$_i^{+1}$	−0.827
	V$_{Cl}^{+1}$+Pb$_i^0$	0.078
Pb$_I^0$	V$_{Pb}^0$+I$_i^0$	**-0.850**
	V$_{Pb}^{-1}$+I$_i^{+1}$	**-0.170**
Pb$_I^{-3}$	V$_{Pb}^{-2}$+I$_i^{-1}$	2.390
Pb$_I^{-2}$	V$_{Pb}^{-1}$+I$_i^{-1}$	0.850
	V$_{Pb}^{-2}$+I$_i^0$	0.930
I$_{Pb}^0$	V$_I^0$+Pb$_i^0$	−0.360
I$_{Pb}^{+1}$	V$_I^{+1}$+Pb$_i^0$	0.190

that Br$_{Pb}^{+3}$ and Br$_{Pb}^{+2}$ defects decompose most favorably into V$_{Br}^{+1}$ and either Pb$_i^{+1}$ or Pb$_i^{+2}$ thus leaving the only major deep defect, Pb$_i$, which could in turn could dimerize with another Pb atom. These results are in agreement with experimental studies[13] which associate deep electron trapping to Pb$_2$ dimers and Pb cations. Similar analysis for the Pb$_{Cl}$ and Cl$_{Pb}$ species suggests that the only significantly contributing deep defect is the chloride vacancy (V$_{Cl}$). This also sheds light on the question of the role of chloride in the mixed halide perovskites i.e. MAPbI$_{3-x}$Cl$_x$. Having chloride in the mixed perovskite does not introduce additional deep trapping centers. In the case of MAPbI$_3$, one should note that Pb$_I^0$ antisite does not decompose into primitive species such as V$_{Pb}$ and I$_i$, and this makes the Pb$_I$ antisite a major source of deep traps. By looking at Figure 3 it is apparent that the preferred conditions for growth in MAPbBr$_3$ and MAPbCl$_3$ are halide-rich environments. This is opposite to

the pure MAPbI$_3$ case, where I-poor conditions are preferred in order to have trap free crystal.

One way to control the rich/poor growth environment is to choose a lead precursor that brings with it an excess of halide such as PbBr$_2$, PbI$_2$, PbCl$_2$ as used in many studies. Another way to control the richness of halide is to use a halide precursor with relatively low enthalpy of formation such as HBr or HCl. Indeed, it was shown[15] that the best MAPbBr$_3$ films are obtained by adding HBr into solution. As mentioned above, the excess of halide is preferable in case of Br and Cl perovskites, whereas in MAPbI$_3$ one needs to use a mixed[4] halide approach to prevent formation of deep trapping centers.

Finally, we estimate reaction enthalpies (formation enthalpy of the perovskites with respect to initial product precursors) of the interacting precursors to shed light on the stability of the perovskites. Zero reaction enthalpy indicates dynamic equilibrium between coexisting initial precursors and a final perovskite phase. A greater value of enthalpy in the exothermic reaction (PbX$_2$ + MAX → MAPbX$_3$) implies a greater stability of the product perovskite phase. The reaction enthalpy is estimated via

$$\Delta H_f(\mathrm{CH_3NH_3PbX_3}) = \mu_{\mathrm{CH_3NH_3PbX_3}} - \mu_{\mathrm{PbX_2}}^{\mathrm{solid}} - \mu_{\mathrm{CH_3NH_3X}}^{\mathrm{solid}} \tag{3}$$

where X = I, Br, Cl, μ is the chemical potential computed as the DFT energy per corresponding solid unit, and the solid superscript indicates stable solid phases at room temperature and 1 atm. Values computed for MAPbI$_3$, MAPbBr$_3$, and MAPbCl$_3$ were of −0.1, −0.25, and −0.7 eV, respectively. Stability grows as one goes from I to Br to Cl. Even lower values for the reaction enthalpy have previously been reported[10] in MAPbI$_3$ ($\Delta H_f(\mathrm{CH_3NH_3PbI_3})$ = −0.04 eV). Such a low value indicates that the enthalpy gain of MAPbI$_3$ is relatively low with respect to the precursor phases MAI and PbI$_2$, causing the low stability of the perovskite compound.[4] This finding implies that the final perovskite compound is prone to destabilization in the regime of moderate energy supplying mechanisms such as thermal degradation and light soaking. On the other hand, MAPbBr$_3$ has a higher reaction enthalpy, and MAPbCl$_3$ is the most stable. We have performed XRD experiments to track the evolution of the representative perovskite Bragg peaks as a function of time for 7 days in ambient atmosphere. Results are reported in Figure 5 for MAPbI$_3$, MAPbBr$_3$, and MAPbCl$_3$. From Figure 5, the PbI$_2$ peak appears immediately, and this correlates well with phase coexistence between MAPbI$_3$ and (MAI with PbI$_2$). On the
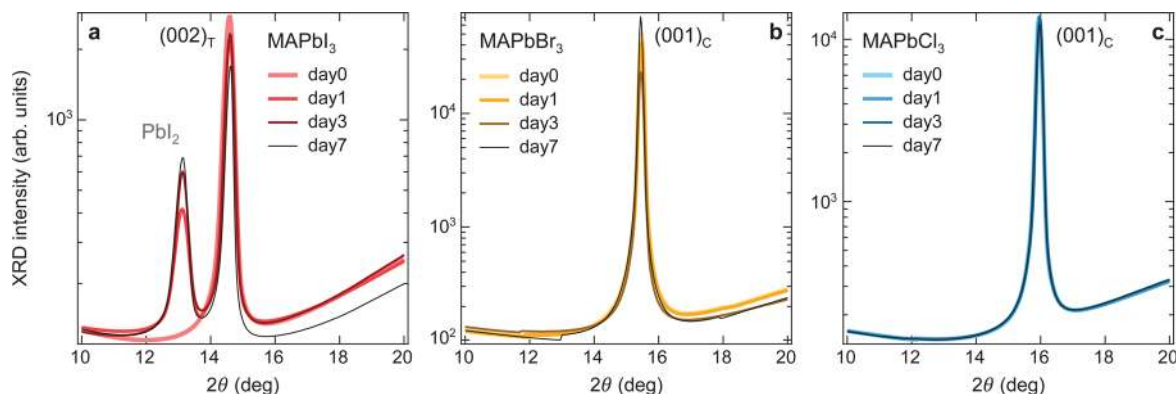
Figure 5. Time evolution of the main XRD peak of the perovskite phase for: (a) MAPbI$_3$, (b) MAPbBr$_3$, and (c) MAPbCl$_3$.

other hand, no additional features are found over time for $MAPbBr_3$ and $MAPbCl_3$ films, consistent with our theoretical finding of stable $MAPbBr_3$ and $MAPbCl_3$ perovskites.

Table 2 summarizes our main findings.

Table 2. Summary of Main Findings

key findings	$MAPbI_3$	$MAPbBr_3$	$MAPbCl_3$
preferred growth mode (PGM)	I-poor	Br-rich	Cl-rich
major source of deep defects	Pb_I	Pb_I, V_{Br}	V_{Cl}
concentration of deep defects at PGM	0	0, 1×10^7 cm^{-3}	1×10^5 cm^{-3}
good values for the E_F at PGM (eV)	0.8–1.8	0.25–2.22	0–2.6
reaction enthalpy	−0.1	−0.25	−0.7
stability	poor	good	best

The results presented in this study provide a unified view of the defect physics in the most common organometal halide perovskites. They are summarized in Table 2. Good values for the E_F in PGM are defined as values of the Fermi level at which defect formation energy is sufficiently high to ensure significantly low defect concentrations ($<1 \times 10^{12}$ cm^{-3}). The investigations demonstrate the effect of halide replacement on electronic structure and perovskite stability. Analysis of defect aggregation in terms of defect binding energies reveals that the major source of deep traps is markedly different for the distinct perovskite materials.

METHODS

Calculations were performed within DFT formalism using the Perdew–Burke–Ernzerhof (PBE)[30] GGA exchange correlation functional. Calculations were performed with the help of the CP2K[31] package within Gaussian-augmented plane waves (GAPW) dual basis set using the molecularly optimized MOLOPT[31] double ζ-valence polarized (mDZVP) basis set implemented in CP2K code, which has very small BSSE errors in gas and condensed phases.[4,32−35] The plane-wave cutoff was 300 Ry, which is suitable for the Goedecker−Teter−Hutter pseudopotentials.[36] Periodic boundary conditions were used in all calculations. Spin-polarized (LSDA) and spin-unpolarized caculations (LDA) were performed in the case of the odd−even number of electrons. The structural minimization was performed with the help of the Broyden-Fletcher-Goldfarb-Shanno algorithm[37] (BFGS). Lattice constants were optimized and used throughout the calculations. The structural optimiziation was considered converged if the forces acting on the atoms were less than 0.04 eV·Å^{-1}. CP2K is a Γ-point code, therefore a sufficient number of unit cells is required to guarantee the convergence. For the $MAPbI_3$ material we have used $3 \times 3 \times 4$ supercell (1728 atoms) of the original tetragonal unit cell, whereas for the $MAPbBr_3$ and $MAPbCl_3$ we have used $4 \times 4 \times 4$ supercell composed of the original cubic cell. It was found that energy per primitive unit cell has converged to the error less than 10 meV/u.cell in all cases. In additional, in case of the $MAPbBr_3$ and $MAPbCl_3$ $4 \times 4 \times 4$ is the natural choice because these are direct gap materials but bandgap is located at the R ((1/2), (1/2), (1/2))[38,39] point in Brillouin zone and this choice correctly zone folds the R point onto the Γ point. Spin−orbit coupling (SOC) effectd in the calculations of the defect formation energies have been discussed[4] and have found to possess negligible contributions along with BSSE errors. All necessary corrections in defect formation energy calculations and detailed calculation procedure can be found elsewhere.[4] Unit-cell parameters used for the tetragonal $MAPbI_3$ can be found in ref 4. whereas for $MAPbBr_3$ and $MAPbCl_3$, they are $a = 6.02$ Å and $a = 5.80$ Å, respectively.

It was found previously[20] that successful DFT bandgap prediction relies on neglecting the spin−orbital coupling (SOC). Some works[40,41] found that SOC inclusion has an effect both on VBM and CBM, with a huge impact on the latter, while modifying dispersion on top of the VBM. There are also direct small SOC effect consequences to the estimations of ground state properties such as structure, lattice constants and energetics.[4,28,42,43] Recently, the role the hybrid exchange correlation functionals with screened exchange, such as Heyd−Scuseria−Ernzerhof[44,45] (HSE), has been emphasized.[46] It was found that the fraction of the exchange can change the location of the VBM in $MAPbI_3$ with respect to the average electrostatic potential, which in turn may affect the position of the defect transition levels. While this holds true for hybrid exchange correlation functionals in general,[47] it is still questionable when using various types of the DFT-hybrids such as PBE0 and HSE. For the example of $MAPbI_3$, it was shown to predict the location of the VBM with an error of 0.33 eV,[48] which could also affect the defect transition levels. We have therefore estimated the self-interaction correction (SIC)[49−51] for the $MAPbI_3$ system, which is due to self-interaction between single electrons and partially taken into account in hybrid DFT calculations. It gave us a value of −0.87 eV for the VBM downshift, which is comparable to previously published results[48] of the PBE hybrid (PBE0)[52] vs Perdew−Burke−Ernzerhof (PBE)[30] of −0.75 eV. This indicates that the usage of hybrid DFT schemes alone is not a complete solution to the bandgap and defect transition level problem. Indeed, recently it was shown that calculations at the hybrid DFT level, namely HSE+SOC, for $MAPbCl_3$, $MAPbBr_3$ and $CsPbBr_3$[22,43,53] indicate that they cannot reproduce bandgap correctly, only GW[40,54,55]-like calculations can correctly address this problem.[53] Experimental bandgap in the case of $MAPbCl_3$ is estimated[56] to be 2.94 eV, which makes our calculated value of 2.52 eV close enough compared to other higher level hybrid DFT levels.[57] Given the wide spread of results from prior works at the hybrid DFT level, that absolute ionization potentials give reasonable values compared to the experimental ones,[24,40,58] and that theoretical predictions at the semilocal level agree with experimental data,[4,19,59] there is a large degree of credibility for semilocal DFT calculations of these organo-metal halide systems.

AUTHOR INFORMATION

Corresponding Author

*E-mail: ted.sargent@utoronto.ca.

Notes

The authors declare no competing financial interest.

REFERENCES

(1) Kim, H.-S.; Lee, C.-R.; Im, J.-H.; Lee, K.-B.; Moehl, T.; Marchioro, A.; Moon, S.-J.; Humphry-Baker, R.; Yum, J.-H.; Moser, J. E.; et al. Lead Iodide Perovskite Sensitized All-Solid-State Submicron Thin Film Mesoscopic Solar Cell with Efficiency Exceeding 9%. *Sci. Rep.* **2012**, 2, 591.

(2) Lee, M. M.; Teuscher, J.; Miyasaka, T.; Murakami, T. N.; Snaith, H. J. Efficient Hybrid Solar Cells Based on Meso-Superstructured Organometal Halide Perovskites. *Science* **2012**, 338, 643−647.

(3) Burschka, J.; Pellet, N.; Moon, S.-J.; Humphry-Baker, R.; Gao, P.; Nazeeruddin, M. K.; Grätzel, M. Sequential Deposition as a Route to High-Performance Perovskite-Sensitized Solar Cells. *Nature* **2013**, *499*, 316−319.

(4) Buin, A.; Pietsch, P.; Xu, J.; Voznyy, O.; Ip, A. H.; Comin, R.; Sargent, E. H. Materials Processing Routes to Trap-Free Halide Perovskites. *Nano Lett.* **2014**, *14*, 6281−6286.

(5) Kim, J.; Lee, S.-H.; Lee, J. H.; Hong, K.-H. The Role of Intrinsic Defects in Methylammonium Lead Iodide Perovskite. *J. Phys. Chem. Lett.* **2014**, *5*, 1312−1317.

(6) Menéndez-Proupin, E.; Palacios, P.; Wahnón, P.; Conesa, J. C. Self-Consistent Relativistic Band Structure of the $CH_3NH_3PbI_3$ Perovskite. *Phys. Rev. B* **2014**, *90*, 045207.

(7) Miller, E. M.; Zhao, Y.; Mercado, C.; Saha, S.; Luther, J. M.; Zhu, K.; Stevanovic, V.; Perkins, C. L.; van de Lagemaat, J. Substrate-Controlled Band Positions in $CH_3NH_3PbI_3$ Perovskite Films. *Phys. Chem. Chem. Phys.* **2014**, *16*, 22122−22130.

(8) Xing, G.; Mathews, N.; Sun, S.; Lim, S. S.; Lam, Y. M.; Gratzel, M.; Mhaisalkar, S.; Sum, T. C. Long-Range Balanced Electron- and Hole-Transport Lengths in Organic-Inorganic $CH_3NH_3PbI_3$. *Science* **2013**, *342*, 344−347.

(9) Yin, W.-J.; Shi, T.; Yan, Y. Unique Properties of Halide Perovskites as Possible Origins of the Superior Solar Cell Performance. *Adv. Mater.* **2014**, *26*, 4653−4658.

(10) Haruyama, J.; Sodeyama, K.; Han, L.; Tateyama, Y. Termination Dependence of Tetragonal $CH_3NH_3PbI_3$ Surfaces for Perovskite Solar Cells. *J. Phys. Chem. Lett.* **2014**, *5*, 2903−2909.

(11) Yin, W.-J.; Shi, T.; Yan, Y. Unusual Defect Physics in $CH_3NH_3PbI_3$ Perovskite Solar Cell Absorber. *Appl. Phys. Lett.* **2014**, *10*, 063903.

(12) Stranks, S. D.; Eperon, G. E.; Grancini, G.; Menelaou, C.; Alcocer, M. J. P.; Leijtens, T.; Herz, L. M.; Petrozza, A.; Snaith, H. J. Electron-Hole Diffusion Lengths Exceeding 1 Micrometer in an Organometal Trihalide Perovskite Absorber. *Science* **2013**, *342*, 341−344.

(13) Shkrob, I. A.; Marin, T. W. Charge Trapping in Photovoltaically Active Perovskites and Related Halogenoplumbate Compounds. *J. Phys. Chem. Lett.* **2014**, *5*, 1066−1071.

(14) Schmidt, L. C.; Pertegás, A.; González-Carrero, S.; Malinkiewicz, O.; Agouram, S.; Minguez Espallargas, G.; Bolink, H. J.; Galian, R. E.; Pérez-Prieto, J. Nontemplate Synthesis of $CH_3NH_3PbBr_3$ Perovskite Nanoparticles. *J. Am. Chem. Soc.* **2014**, *136*, 850−853.

(15) Heo, J. H.; Song, D. H.; Im, S. H. Planar $CH_3NH_3PbBr_3$ Hybrid Solar Cells with 10.4% Power Conversion Efficiency, Fabricated by Controlled Crystallization in the Spin-Coating Process. *Adv. Mater.* **2014**, *26*, 8179−8183.

(16) Zhang, M.; Yu, H.; Lyu, M.; Wang, Q.; Yun, J.-H.; Wang, L. Composition-Dependent Photoluminescence Intensity and Prolonged Recombination Lifetime of Perovskite $CH_3NH_3PbBr_{3-x}Cl_x$ films. *Chem. Commun.* **2014**, *50*, 11727−11730.

(17) Liu, M.; Johnston, M. B.; Snaith, H. J. Efficient Planar Heterojunction Perovskite Solar Cells by Vapour Deposition. *Nature* **2013**, *501*, 395−398.

(18) Du, M. H. Efficient Carrier Transport in Halide Perovskites: Theoretical Perspectives. *J. Mater. Chem. A* **2014**, *2*, 9091−9098.

(19) Shi, T.; Yin, W.-J.; Hong, F.; Zhu, K.; Yan, Y. Unipolar Self-Doping Behavior in Perovskite $CH_3NH_3PbBr_3$. *Appl. Phys. Lett.* **2015**, *106*, 103902.

(20) Mosconi, E.; Amat, A.; Nazeeruddin, M. K.; Gratzel, M.; de Angelis, F. First-Principles Modeling of Mixed Halide Organometal Perovskites for Photovoltaic Applications. *J. Phys. Chem. C* **2013**, *117*, 13902−13913.

(21) Amat, A.; Mosconi, E.; Ronca, E.; Quarti, C.; Umari, P.; Nazeeruddin, M. K.; Gratzel, M.; De Angelis, F. Cation-Induced Band-Gap Tuning in Organohalide Perovskites: Interplay of Spin-Orbit Coupling and Octahedra Tilting. *Nano Lett.* **2014**, *14*, 3608−3616.

(22) Giorgi, G.; Fujisawa, J.-I.; Segawa, H.; Yamashita, K. Cation Role in Structural and Electronic Properties of 3D Organic-Inorganic Halide Perovskites: A DFT Analysis. *J. Phys. Chem. C* **2014**, *118*, 12176−12183.

(23) Butler, K. T.; Frost, J. M.; Walsh, A. Band Alignment of the Hybrid Halide Perovskites $CH_3NH_3PbCl_3$, $CH_3NH_3PbBr_3$ and $CH_3NH_3PbI_3$. *Mater. Horiz.* **2015**, *2*, 228−231.

(24) Even, J.; Pedesseau, L.; Jancu, J.-M.; Katan, C. Importance of Spin-Orbit Coupling in Hybrid Organic/Inorganic Perovskites for Photovoltaic Applications. *J. Phys. Chem. Lett.* **2013**, *4*, 2999−3005.

(25) Ryu, S.; Noh, J. H.; Jeon, N. J.; Chan Kim, Y.; Yang, W. S.; Seo, J.; Seok, S. I. Voltage Output of Efficient Perovskite Solar Cells With High Open-Circuit Voltage and Fill Factor. *Energy Environ. Sci.* **2014**, *7*, 2614−2618.

(26) Van de Walle, C. G.; Neugebauer, J. First-Principles Calculations for Defects and Impurities: Applications to III-nitrides. *J. Appl. Phys.* **2004**, *95*, 3851−3879.

(27) Shi, H.; Du, M.-H. Shallow Halogen Vacancies in Halide Optoelectronic Materials. *Phys. Rev. B* **2014**, *90*, 174103.

(28) Kim, J.; Lee, S.-C.; Lee, S.-H.; Hong, K.-H. Importance of Orbital Interactions in Determining Electronic Band Structures of Organo-Lead Iodide. *J. Phys. Chem. C* **2015**, *119*, 4627−4634.

(29) Duan, X. M.; Stampfl, C. Vacancies and Interstitials in Indium Nitride: Vacancy Clustering and Molecular Bondlike Formation from First Principles. *Phys. Rev. B* **2009**, *79*, 174202.

(30) Perdew, J. P.; Burke, K.; Ernzerhof, M. Generalized Gradient Approximation Made Simple. *Phys. Rev. Lett.* **1996**, *77*, 3865−3868.

(31) VandeVondele, J.; Hutter, J. Gaussian Basis Sets for Accurate Calculations on Molecular Systems in Gas and Condensed Phases. *J. Chem. Phys.* **2007**, *127*, 114105.

(32) Leitsmann, R.; Böhm, O.; Plänitz, P.; Radehaus, C.; Schaller, M.; Schreiber, M. Adsorption Mechanisms of Fluorocarbon Polymers at Ultra Low-k Surfaces. *Surf. Sci.* **2010**, *604*, 1808−1812.

(33) Takaluoma, T. T.; Laasonen, K.; Laitinen, R. S. Molecular Dynamics Simulation of the Solid-State Topochemical Polymerization of S_2N_2. *Inorg. Chem.* **2013**, *52*, 4648−4657.

(34) Bork, N.; Loukonen, V.; Vehkamäki, H. Reactions and Reaction Rate of Atmospheric SO_2 and $O_3^-(H_2O)_n$ Collisions via Molecular Dynamics Simulations. *J. Phys. Chem. A* **2013**, *117*, 3143−3148.

(35) Smecca, E.; Motta, A.; Fragalà, M. E.; Aleeva, Y.; Condorelli, G. G. Spectroscopic and Theoretical Study of the Grafting Modes of Phosphonic Acids on ZnO Nanorods. *J. Phys. Chem. C* **2013**, *117*, 5364−5372.

(36) Hartwigsen, C.; Goedecker, S.; Hutter, J. Relativistic Separable Dual-Space Gaussian Pseudopotentials from H to Rn. *Phys. Rev. B* **1998**, *58*, 3641−3662.

(37) Press, W. H.; Teukolsky, S. A.; Vetterling, W. T.; Flannery, B. P. *Numerical Recipes: The Art of Scientific Computing*, 3rd ed; Cambridge University Press: New York, 2007.

(38) Jishi, R. A.; Ta, O. B.; Sharif, A. A. Modeling of Lead Halide Perovskites for Photovoltaic Applications. *J. Phys. Chem. C* **2014**, *118*, 28344−28349.

(39) Grote, C.; Ehrlich, B.; Berger, R. F. Tuning the Near-Gap Electronic Structure of Tin-Halide and Lead-Halide Perovskites via Changes in Atomic Layering. *Phys. Rev. B* **2014**, *90*, 205202.

(40) Brivio, F.; Butler, K. T.; Walsh, A.; van Schilfgaarde, M. Relativistic Quasiparticle Self-Consistent Electronic Structure of Hybrid Halide Perovskite Photovoltaic Absorbers. *Phys. Rev. B* **2014**, *89*, 155204.

(41) Giorgi, G.; Fujisawa, J.-I.; Segawa, H.; Yamashita, K. Small Photocarrier Effective Masses Featuring Ambipolar Transport in Methylammonium Lead Iodide Perovskite: A Density Functional Analysis. *J. Phys. Chem. Lett.* **2013**, *4*, 4213−4216.

(42) Agiorgousis, M. L.; Sun, Y.-Y.; Zeng, H.; Zhang, S. Strong Covalency-Induced Recombination Centers in Perovskite Solar Cell Material $CH_3NH_3PbI_3$. *J. Am. Chem. Soc.* **2014**, *136*, 14570−14575.

(43) Lang, L.; Yang, J.-H.; Liu, H.-R.; Xiang, H.; Gong, X. First-Principles Study on the Electronic and Optical Properties of Cubic $\{ABX_3\}$ Halide Perovskites. *Phys. Lett. A* **2014**, *378*, 290−293.

(44) Heyd, J.; Scuseria, G. E.; Ernzerhof, M. Hybrid Functionals Based on a Screened Coulomb Potential. *J. Chem. Phys.* **2003**, *118*, 8207−8215.

(45) Heyd, J.; Scuseria, G. E.; Ernzerhof, M. Erratum: Hybrid Functionals Based on a Screened Coulomb Potential. *J. Chem. Phys.* **2003**, *118*, 8207; *J. Chem. Phys.* **2006**, *124*, 219906.

(46) Du, M.-H. Density Functional Calculations of Native Defects in $CH_3NH_3PbI_3$: Effects of Spin-Orbit Coupling and Self-Interaction Error. *J. Phys. Chem. Lett.* **2015**, *6*, 1461−1466.

(47) Alkauskas, A.; Broqvist, P.; Pasquarello, A. Defect Levels Through Hybrid Density Functionals: Insights and Applications. *Phys. Status Solidi (b)* **2011**, *248*, 775−789.

(48) Menéndez-Proupin, E.; Palacios, P.; Wahnón, P.; Conesa, J. C. Self Consistent Relativistic Band Structure of the $CH_3NH_3PbI_3$ Perovskite. *Phys. Rev. B* **2014**, *90*, 045207.

(49) Perdew, J. P.; Zunger, A. Self-Interaction Correction to Density-Functional Approximations for Many-Electron Systems. *Phys. Rev. B* **1981**, *23*, 5048−5079.

(50) Legrand, C.; Suraud, E.; Reinhard, P.-G. Comparison of Self-Interaction-Corrections for Metal Clusters. *J. Phys. B: At., Mol. Opt. Phys.* **2002**, *35*, 1115.

(51) Ciofini, I.; Chermette, H.; Adamo, C. A Mean-Field Self-Interaction Correction in Density Functional Theory: Implementation and Validation for Molecules. *Chem. Phys. Lett.* **2003**, *380*, 12−20.

(52) Perdew, J. P.; Ernzerhof, M.; Burke, K. Rationale for Mixing Exact Exchange with Density Functional Approximations. *J. Chem. Phys.* **1996**, *105*, 9982−9985.

(53) Melissen, S. T. A. G.; Labat, F.; Sautet, P.; Le Bahers, T. Electronic Properties of $PbX_3CH_3NH_3$ (X = Cl, Br, I) Compounds for Photovoltaic and Photocatalytic Applications. *Phys. Chem. Chem. Phys.* **2015**, *17*, 2199−2209.

(54) Hedin, L. New Method for Calculating the One-Particle Green's Function with Application to the Electron-Gas Problem. *Phys. Rev.* **1965**, *139*, A796−A823.

(55) Paolo, U.; Edoardo, M.; Filippo, D. A. Relativistic GW calculations on $CH_3NH_3PbI_3$ and $CH_3NH_3SnI_3$ Perovskites for Solar Cell Applications. *Sci. Rep.* **2014**, *4*, 4467.

(56) Dimesso, L.; Dimamay, M.; Hamburger, M.; Jaegermann, W. Properties of $CH_3NH_3PbX_3$ (X = I, Br, Cl) Powders as Precursors for Organic/Inorganic Solar Cells. *Chem. Mater.* **2014**, *26*, 6762−6770.

(57) Yin, W.-J.; Yan, Y.; Wei, S.-H. Anomalous Alloy Properties in Mixed Halide Perovskites. *J. Phys. Chem. Lett.* **2014**, *5*, 3625−3631.

(58) Brgoch, J.; Lehner, A. J.; Chabinyc, M.; Seshadri, R. Ab Initio Calculations of Band Gaps and Absolute Band Positions of Polymorphs of $RbPbI_3$ and $CsPbI_3$: Implications for Main-Group Halide Perovskite Photovoltaics. *J. Phys. Chem. C* **2014**, *118*, 27721−27727.

(59) Xu, J.; Buin, A.; Ip, A. H.; Li, W.; Voznyy, O.; Comin, R.; Yuan, M.; Jeon, S.; Ning, Z.; McDowell, J. J. e. a. Perovskite-fullerene hybrid materials suppress hysteresis in planar diodes. *Nat. Commun.* **2015**, *6*, 7081.

(60) Loken, C.; Gruner, D.; Groer, L.; Peltier, R.; Bunn, N.; Craig, M.; Henriques, T.; Dempsey, J.; Yu, C.-H.; Chen, J.; Dursi, L. J.; et al. SciNet: Lessons Learned from Building a Power-efficient Top-20 System and Data Centre. *J. Phys.: Conf. Ser.* **2010**, *256*, 012026.